Biosensors and Bioelectronics 131 (2019) 17–23

Contents lists available at ScienceDirect

Biosensors and Bioelectronics

journal homepage: www.elsevier.com/locate/bios

Paper based modification-free photoelectrochemical sensing platform with single-crystalline aloe like TiO_2 as electron transporting material for cTnI detection

Chaomin Gao[a], Jie Xue[a], Lina Zhang[b], Peini Zhao[a,*], Kang Cui[a], Shenguang Ge[c,*], Jinghua Yu[a]

[a] School of Chemistry and Chemical Engineering, University of Jinan, Jinan, Shandong 250022, PR China
[b] Shandong Provincial Key Laboratory of Preparation and Measurement of Building Materials, University of Jinan, Jinan 250022, PR China
[c] Institute for Advanced Interdisciplinary Research, University of Jinan, Jinan 250022, PR China

ARTICLE INFO

Keywords:
Paper based analytical device
Photoelectrochemical
Modification-free
TiO_2

ABSTRACT

By controlling target-induced signal quencher release, a label-free and modification-free microfluidic paper based photoelectrochemical analytical device (μ-PAD) for cardiac troponin-I (cTnI) detection was designed for the first time. To achieve it, cellulose paper based single-crystalline three-dimensional aloe like TiO_2 arrays (PSATs) were firstly fabricated as the electron transporting material, providing direct pathways for the charge carriers transfer, and subsequently coupled with CdS to form PSATs/CdS heterojunction for extending the solar spectrum response. Meanwhile, positive charged mesoporous silica nanoparticles (PMSNs) were prepared as the nanocarrier to efficient entrap the Cu^{2+} which could be regarded as signal quencher due to their reaction with CdS to form Cu_xS. Single stranded DNAs (ssDNAs), which could bind specifically with the target of cTnI, were then introduced to couple with the PMSNs and used as the bio-gate to encapsulate the signal quencher of Cu^{2+}, endowing the functional PMSNs with responsiveness to cTnI. When the cTnI existed, the ssDNAs were dissociated from PMSNs due to the formation of cTnI-ssDNAs complexes, triggering controllable release of the trapped Cu^{2+}, and further decreasing the photocurrent signal caused by the formation of Cu_xS. Accordingly, the concentration of cTnI could be accurately quantified via the photocurrent, realizing the target-induced modification-free μ-PAD assay. We believe this work could provide an ingenious idea to construct the easy-to-use novel modification-free μ-PAD.

1. Introduction

Due to the alluring characteristics of being chemically modifiable, easily biodegradable, and excellent flexible, cellulose paper, as a great stationery invented 2000 years ago, has attracted considerable attention in the last decade (Gao et al., 2018a; Scala-Benuzzi et al., 2018; Wang et al., 2017). In particular, the cellulose paper can offer an outstanding matrix for nanomaterials growth and generate various functionalized surfaces with admirable characteristics, making it more appealing to fabrication of portable, easy-to-use, and low-cost analytical device (Cate et al., 2014; Kokkinos et al., 2018; Martinez et al., 2007). Beyond this, owing to the simple fabrication processes and efficient combination with numerous analytical technologies including chemiluminescence (Yu et al., 2011), electrochemiluminescence (Gao et al., 2015), and Raman spectroscopy (Li et al., 2018), paper based analytical devices qualify for a promising candidate for developing novel portable analytical sensing platform with highly sensitivity (Scala-Benuzzi et al., 2018; Wang et al., 2012; Gao et al., 2018b). Especially, microfluidic paper based photoelectrochemical analytical device (μ-PAD) with the features of high sensitive, cost-effective, and user-friendly for portable bioassays has attracted increasing attention (Wu et al., 2013). Although the established μ-PADs have made great progress, to our knowledge, as for the existing constructed μ-PADs, the immobilization of bio-recognition probes is the prerequisite step, which could be affected by multiple factors and unavoidably complicated the experimental processes. For example, the orientation and density of the immobilized probes should be exactly controlled in order to achieve the sensitivity detection. In addition, the configurational freedom of the immobilized probes is restricted and even their geometry maybe changed in the immobilization processes owing to the steric hindrance effect (Yu and Lai, 2013), inevitably leading to the much lower binding rate and efficiency than that in solution. Therefore, it is reasonable and urgent to draw up a new strategy to avoid the step of bio-probes immobilization in the development of high-performance μ-PADs. In contrast with

* Corresponding authors.
E-mail addresses: zhaopn_1985@163.com (P. Zhao), chm_gesg@163.com (S. Ge).

https://doi.org/10.1016/j.bios.2019.01.038
Received 9 December 2018; Received in revised form 4 January 2019; Accepted 21 January 2019
Available online 25 January 2019

heterogeneous bioassays, modification-free bioassays, which require neither steps of separating antigen or antibody from the samples nor washing, endow the bioassays with appealing simplicity, rapid response, and high sensitivity (Lee et al., 2012). What's more, modification-free bioassays have the merits of time-saving and improved recognition efficiency (Yang et al., 2017). Therefore, integrating modification-free strategy with paper based analytical devices is of great significance to promote the further development of μ-PADs. For this purpose, in this work, a label-free and modification-free μ-PAD was designed for cardiac troponin I (cTnI) sensing which is a biomarker for acute myocardial infarction (AMI) (Korff et al., 2006).

Indubitably, photoactive species functionalized the cellulose paper, as a necessary requisite to achieve the desirable photocurrent signal in the μ-PAD, determine the analytical performance of μ-PAD. In principle, the desired photoactive materials should be with appropriate band gap, high carrier mobility, and relatively low cost. TiO_2, as a promising candidate, has been proved to be an excellent photoactive material due to its good photoelectric activity, chemical stability, and biocompatibility (Ai et al., 2015; Gao et al., 2017; Liu et al., 2016). Until now, although various structural morphologies of paper based TiO_2 including zero-dimension (Li et al., 2014a) and two-dimension nanosheets (Li et al., 2014b) have been successfully prepared, they are seldom met the requirement of sensitive bioanalysis application due to their intrinsic properties with the lack of the photocurrent conversion efficiency and high carrier recombination rate. It is therefore essential to explore more effective TiO_2 nanomaterials for achieving remarkable photocurrent density in bioanalysis process. Single-crystalline TiO_2 with three-dimension (3D) structure, which could offer high surface area, favorable charge separation pathways, and short diffusion length for charge carriers transporting has been demonstrated a suitable strategy to improve the PEC performance of TiO_2 (Butburee et al., 2018). Unfortunately, the single-crystalline 3D TiO_2 has not yet been successful synthesized on cellulose paper. In this work, for the first time, paper based single-crystalline 3D aloe-like TiO_2 arrays (PSATs) were explored with a one-step hydrothermal strategy to serve as the electron transporting material. In addition, a narrow bandgap semiconductor of CdS, possessing a suitable band gap (~2.4 eV), photo and electrochemical stability was used to couple with PSATs for extending the solar spectrum response.

In order to complete the target-induced modification-free μ-PAD, positively charged mesoporous silica nanoparticles (PMSNs) were prepared as a nimble nanocarriers to entrap Cu^{2+} which were capped by the single-stranded DNA aptamers (ssDNAs) due to the electrostatic attraction between ssDNAs and PMSNs. The ssDNAs rationally serve as bio-gate to block the Cu^{2+} loaded into PMSNs. When cTnI exists, the entrapped Cu^{2+} could be released by the liberation of ssDNAs from PMSNs caused by the specific interaction between cTnI and ssDNAs which is more competitive than the electrostatic attraction between PMSNs and ssDNAs (Gu et al., 2017; Wang et al., 2015), realizing the controlled release of Cu^{2+} (Scheme 1A). The released Cu^{2+} could immediately react with CdS to generate Cu_xS with the formation of new energy levels, serving as trap sites to reduce the photocurrent density (Du et al., 2014; Mei et al., 2018; Wang et al., 2010). Thus, the decreased photocurrent signal is evidently proportional to the concentration of released Cu^{2+}, which is, in turn, varies as the concentration of cTnI. In the absence of cTnI, Cu^{2+} was encapsulated in the PMSNs and a higher photocurrent intensity was observed (Scheme 1B). Overall, the concept of target-induced modification-free μ-PAD was proposed for the first time which could be used for the ultrasensitive detection of cTnI.

2. Experimental section

2.1. Design and preparation of the μ-PAD

Typically, the shape patterns of the μ-PAD were designed with Adobe illustrator CS6 and the preparation processes were shown in Fig. S1. Firstly, waxes were used to construct the hydrophobic barrier. After printed with a wax printer, the paper was heat to melt the waxes through the whole paper to generate an effective hydrophobic barrier (Fig. S1A). Then, the carbon counter electrode and Ag/AgCl reference electrode were printed with screen-printed strategy as shown in Fig. S1B. The details about the processes of screen-printed strategy were shown in Fig. S2. After that the paper substrate was cut into independent device and ready for TiO_2 growth. The paper working zone is the hydrophilic circle region with the diameter of 9 mm (Fig. S1C).

In order to evaluate the hydrophobic property of the wax modified paper, the water contact angles of the pure paper, wax modified paper before and after heating were displayed in Fig. S3. As seen, compared with the pure paper, the water contact angle of wax modified paper before or after heated became larger, resulting from the melted wax infiltrating the matrix of the paper fibers.

2.2. Preparation of single-crystalline PSATs and PSATs/CdS samples

The single-crystalline PSATs were prepared with one-step hydrothermal strategy. Firstly, a layer of Ag was modified onto the paper work zone with screen-printed method to endow its admirable conductivity, followed by polished with an agate lapping hammer to make the surface of Ag/paper smooth which was vital for further growth of TiO_2. Subsequently, a thick TiO_2 seed layer providing nucleation sites was decorated with pulsed laser deposition strategy and the processes were described in the Supplementary Material. Then, 0.35 g potassium titanium oxide oxalate dehydrate was dissolved in ultrapure water (3.0 mL), followed by adding diethylene glycol (15 mL) under continuous stirred for 30 min. After that, the mixture was transferred to a Teflon-lined stainless steel autoclave, where the Ag/paper substrate was placed with the conductivity side facing down. The autoclave was hydrothermally treated at 110 °C for 8 h under autogenously pressure. After cooling to room temperature, the sample was taken out and rinsed thoroughly with ultrapure water, drying in ambient air at 80 °C.

PSATs/CdS sample was obtained with the chemical bath deposition strategy and the details were in Supplementary Material.

2.3. Preparation of positively charged mesoporous silica nanoparticles

Mesoporous silica nanoparticles (MSNs) were synthesized according to the previous literatures with some modifications (Zhang et al., 2013; Gai et al., 2018). Initially, 0.6 mmol of CTAB was dissolved in 100 mL of ultrapure water, followed by added of sodium hydroxide (2.0 M, 0.8 mL) with stirring at 80 °C. After 30 min, 1 mL of TEOS was dropped in the above solution under vigorously stirred for 2 h. Subsequently, the obtain white precipitate products were washed with methanol and ultrapure water. After that, 0.2 g of products were refluxed for 12 h with the 3 mL of HCl and 150 mL methanol. Finally, the prepared MSNs were filtered and washed thoroughly, followed by dried at 80 °C for 4 h. Then, 20 mg of the MSNs were added into ethanol (5 mL) under sonication, followed by dropped of APTES (1 mL) and stirred for 8 h. In this way, the amine groups were modified onto the surface of MSNs, leading to the formation of positively charged amine-functionalized MSNs (PMSNs). At last, the mixture was centrifugation and washed thoroughly with ethanol and ultrapure water.

2.4. Loading of Cu^{2+} into ssDNAs-capped PMSNs

30 mg of as-prepared PMSNs were added into 10 mL of 100 mM Cu^{2+} solution with shaking for 24 h at room temperature. During this process, Cu^{2+} was entered the pores of the PMSNs through diffusion. Then, 100 μL of ssDNAs (10 nM) were added with stirring for 6 h at room temperature, which could be attached onto the surface of PMSNs through electrostatic interaction and formed the bio-gate. Subsequently, the mixture was centrifuged and washed thoroughly to

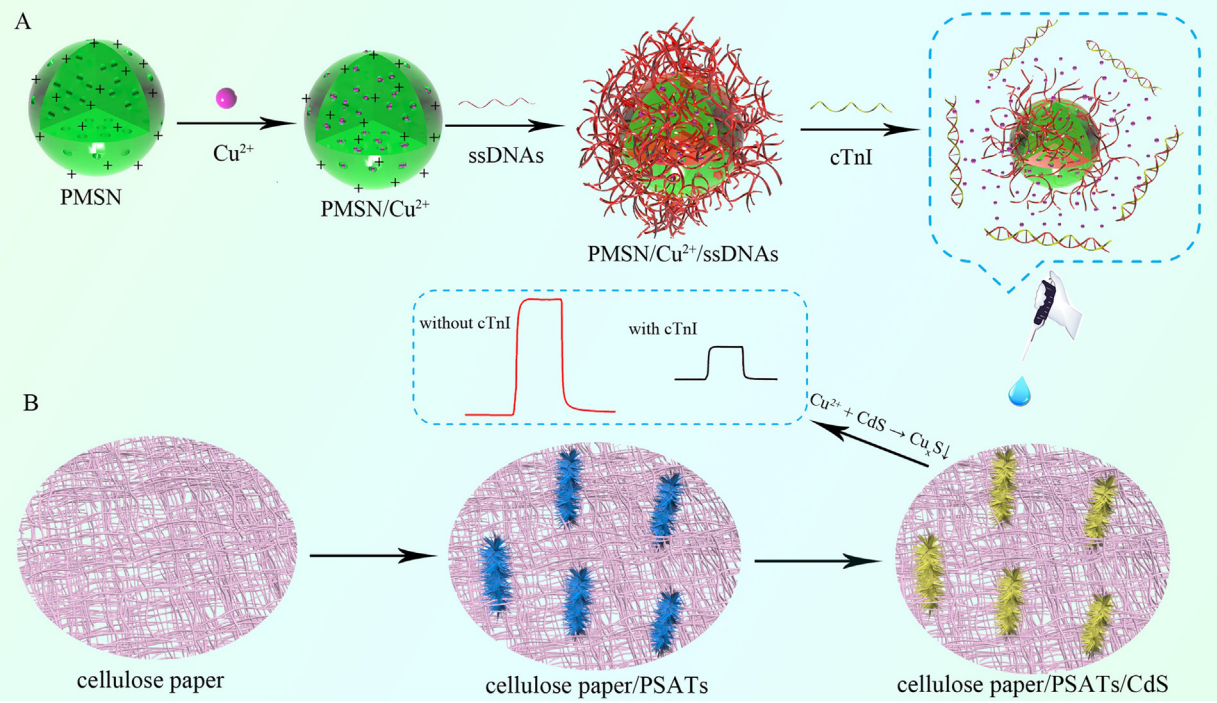

Scheme 1. Schematic principle of the modification-free μ-PAD. (A) The processes of preparation of PMSN/Cu^{2+}/ssDNAs. (B) The processes of cTnI detection.

remove any unloading Cu^{2+}. Finally, the obtained product was re-suspended into 10 mL of Tris-HCl buffer (pH 7.4, containing 0.1 M NaCl).

2.5. Assay procedures of the modification-free μ-PAD

A modification-free μ-PAD sensing platform was constructed with the aid of PMSNs and the assay processes are shown in Scheme 1. When without the target of cTnI, 50 μL of ssDNAs-capped PMSNs loaded with Cu^{2+} was added onto the surface of PSATs/CdS photoelectrode (Scheme 1A), then the photocurrent was measured. When with cTnI, 10 μL of cTnI with different concentrations were incubated with 50 μL of ssDNAs-capped PMSNs at 37 °C for 4 h, and then the mixture was added onto the surface of PSATs/CdS photoelectrode for photocurrent detection. The ascorbic acid was used as the electron donor.

3. Results and discussion

3.1. Characterization of PSATs and PSATs/CdS

The morphologies of the obtained samples were firstly characterized by field-emission scanning electron microscope (FESEM). SEM image showed that the porous network of numerously intertwined cellulose fibers form the paper substrate (Fig. 1A). After modified with a layer of Ag through screen-printed method, the fibers were covered and the surface became smooth compared with pure paper (inset of Fig. 1A). The PSATs uniformly coated on the surface of paper with vertical alignment configuration, as shown in Fig. 1B. Observed at high magnification SEM image, the plenty of branches developed from the backbones to form the 3D aloe like structure, with an average diameter was about 300 nm (Fig. 1C). After decoration with CdS, an enhancement in the surface roughness and topographical changes were observed (Fig. 1D), implying the successfully preparation of PSATs/CdS. To investigate the phase component of the samples, the XRD measurements were carried out (Fig. S4). The peaks located at 37.8° and 64.2° belonged to the anatase TiO_2 (JCPDS-ICDD, 02–0387). While the peak at around 26.5° was assigned to the (002) diffraction of wurtzite CdS (JCPDS No. 41–1049) (He et al., 2018). The chemical composition of the PSATs/CdS sample was examined by energy-dispersive spectroscopy (EDS) as shown in Fig. S5. In addition, the structure and crystalline nature of the single-crystalline PSATs were further examined by transmission electron microscopy image (TEM). Fig. 1E exhibited a TEM image of one nanosheet of PSATs, where it could be seen that the smaller branched decorated on the surface of nanosheet. The selected area electron diffraction (SAED) pattern (top right in Fig. 1E) confirmed the single crystal structure of as-prepared PSATs. As shown in the high-resolution transmission electron microscopy (HRTEM) image taken near the edge of the PSATs as marked in Fig. 1F, the clearly identified lattice fringe space of 0.35 nm indexed to the d-spacing of TiO_2 (101) crystal planes (Awate et al., 2011; Chang and Wu, 2005).

To further investigate the composition and chemical states of the PSATs/CdS, X-ray photoelectron spectroscope (XPS) characterizations were performed. The XPS survey spectrum of PSATs/CdS revealed that the sample was solely constituted of Ti, O, Cd and S (Fig. S6). As seen from the high resolution XPS spectrum of Ti 2p (Fig. 2A), the strong two peaks of Ti $2p_{3/2}$ and Ti $2p_{1/2}$ centered at about 458.1 and 463.8 eV implied that the presence of Ti^{4+} species rather than Ti^{3+} species in PSATs (Ai et al., 2015). Moreover, as shown in high resolution XPS spectrum of O 1 s (Fig. 2B), there was a shoulder peak around the main O 1 s peak side, indicating there are several kinds of oxygen chemical states coexist including the crystal lattice oxygen (O_L) and hydroxyl oxygen (O_H) (Xu et al., 2011). One peak located at 530.6 was assigned to the O in the TiO_2 crystal lattice, while the other located at 532.5 eV was deemed as the O in chemisorbed water. As shown in Fig. 2C, the two peaks located at 404.9 and 411.6 eV could be assigned to Cd $3d_{5/2}$ and Cd $3d_{3/2}$ of CdS. In addition, the S 2p spectra was divided into two peaks of S $2p_{3/2}$ and S $2p_{1/2}$ at 161.3 and 162.4 eV, which corresponding to S^{2-} of CdS (Fig. 2D) (Li et al., 2009).

3.2. Characterization of photo-induced charge carrier separation property of PSATs/CdS

In order to investigate the photogenerated charge carrier separation behavior of the PSATs/CdS sample, steady state photoluminescence (PL) was carried out with the excitation wavelength of 300 nm. As known, low charge carrier recombination rate leaded to lower PL signal

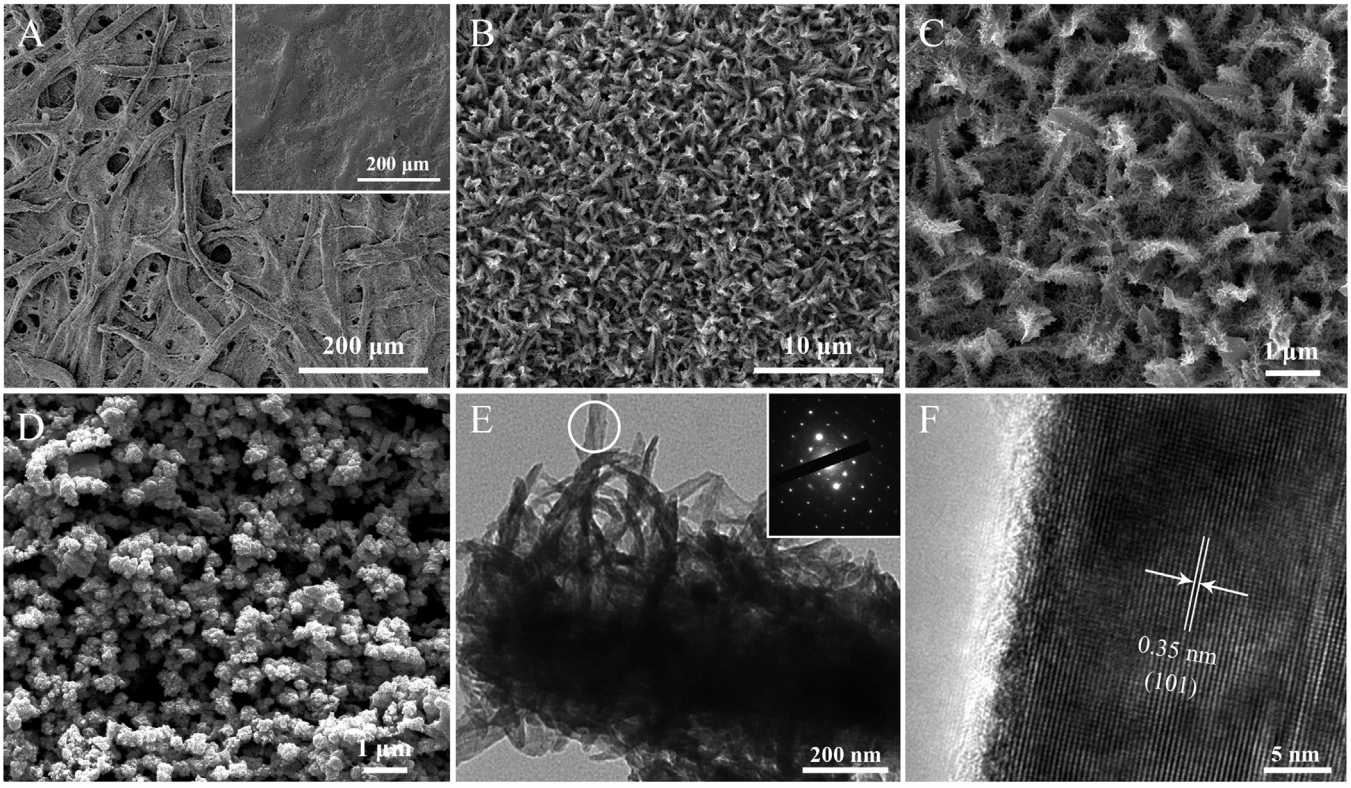

Fig. 1. SEM images of (A) bare cellulose paper (Inset: Ag/paper). Lower (B) and higher magnification (C) of PSATs. (D) PSATs/CdS samples. (E) TEM image of one nanosheet of PSATs (Inset: selected area diffraction of E). (F) HRTEM image of the area marked in (E).

which could qualitatively evaluated the photogenerated charge carrier separation performance (Wu et al., 2010; Zhuang et al., 2016). As illustrated in Fig. 3A, a quite strong PL signal was observed for PSATs (curve a), ascribing to the intrinsic higher electrons and holes recombination rate of TiO_2. When coupled with CdS (curve b), the PL intensity was obviously decreased, which confirmed the formed heterojunction could effectively facilitate the photogenerated carrier separation. To further investigate the photo-induced carrier dynamics at the interfaces between PSATs and CdS, time-resolved photoluminescence (TRPL) was measured with the excitation and emission wavelength of 300 nm and 510 nm, respectively. As shown in Fig. 3B, the curves were fitted with the two exponential function: $F(t) = \Sigma A_i^{\tau/\tau i}$; i = 1, 2, where A_i was prefactor and τ_i was time constant. The average carrier lifetime (τ_{ave}) was estimated with $\tau_{ave} = \Sigma A_i \tau_i^2 / \Sigma A_i \tau_i$; i = 1, 2. The fitted parameters of TRPL spectrum were shown in Table S1. The PSATs/CdS heterojunction decayed faster than the CdS, with PL lifetime of 3.9 ns and 1.25 for the CdS and PSATs/CdS, respectively, further indicating that charge carriers within the CdS could be extracted effectively by PSATs. In addition, the photoresponse was also measured under chopped light illumination with 0 V versus Ag/AgCl. The photoelectrode exhibited sensitively and repeatedly photocurrent responses with the on/off illumination cycles, ascribing to the direct electron transfer pathway provided by the single-crystalline PSATs (Fig. 3C). The photocurrent response of the PSATs/CdS sample was 606 μA cm^{-2} (curve a), which was remarkably enhanced compared to the PSATs 13.6 μA cm^{-2} (curve d), attributing to the PSATs/CdS heterojunction could facilitate the transfer of charge carrier. The photocurrent decreased after the Cu^{2+} added onto the surface of PSATs/CdS photoelectrode (curve b and c), which elucidated that the signal quencher of Cu^{2+} could decrease the photocurrent.

3.3. Growth mechanism of the PSATs

In order to understand the one-step growth processes of PSATs, time-dependent experiments were carried out. SEM observes harvested with different reaction time were shown in Fig. S7. Oriented short and small TiO_2 nanosheets were covered on paper substrate with 2 h (Fig. S7B). When with 4 h reaction time, the 2D plate-like nanostructures TiO_2 were observed (Fig. S7C). As shown in Fig. S7D, by increasing reaction time to 6 h, tiny additional branches could be controlled to selectively growth on the edges of the backbone nanosheet. The sharp surface edges were the preferred nucleation sites for those additional branches due to the relatively large surface free energy (Muller et al., 2000). The needle-shaped branches nanostructures were conspicuous and uniformly distributed on the entire edge of TiO_2 nanosheets backbone, making the surface become rough. If the time prolonged to 8 h, the branches became more numerous and longer, which could greatly enhance the filling rate in the intervals of neighbouring nanosheets (Fig. S7E). With this reaction time, the novel 3D aloe like TiO_2 consisting of TiO_2 nanosheets backbone and short branches were successfully obtained. As seen from Fig. S7F, when the time was 10 h, excessive precursor continues to deposit on the PSATs and it was difficult to distinguish the branched structure.

3.4. Characterization of MSNs

As shown in Fig. 4A, the MSNs exhibited the spherical morphology with the diameter about 80 nm. The TEM image demonstrated that the MSNs had ordered porous structure with diameter of 2–3 nm nanopores (Fig. 4B). In addition, zeta potential was used to characterize the surface charges evolution of functioned MSNs, as shown in Fig. 4C. The zeta potential value of the MSNs was increased from −7.12 to + 41.9 mV after loading of Cu^{2+} and amine-functionalized. Just as expected, after adsorption of negatively charged ssDNAs on PMSNs, the zeta potential value drastically decreased to −51.2 mV. When the target cTnI was added, the zeta potential value could recover to −18.2 mV due to the detachment of the bio-gate ssDNAs. The above results verified that the ability of target-induced control releasing of

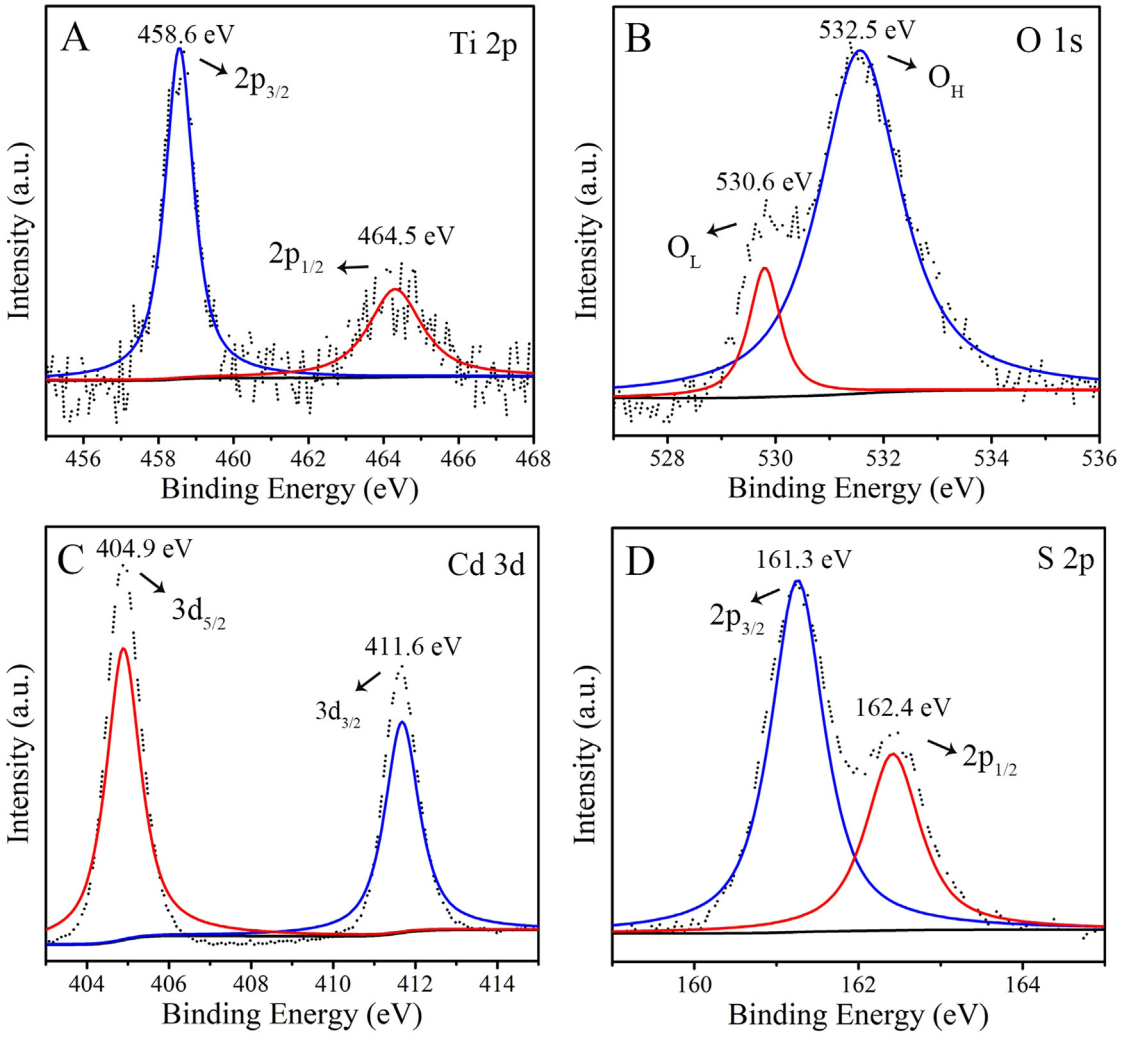

Fig. 2. High resolution XPS spectra of (A) Ti 2p. (B) O 1 s (C) Cd 3d. (D) S 2p. The black short dot curves are the experimental result and the red and blue curves are the fitting results.

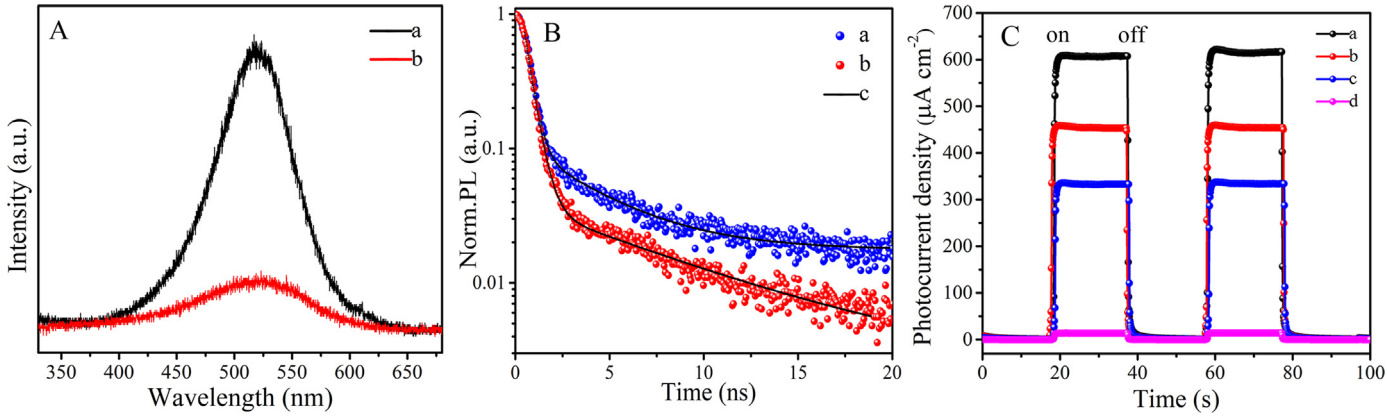

Fig. 3. (A) PL spectra of CdS (curve a) and PSATs/CdS samples (curve b). (B) TRPL spectra of PSATs/CdS (curve a) and CdS samples (curve b). (C) Photocurrent responses of PSATs (curve d), PSATs/CdS (curve a), PSATs/CdS with 0.1 pg mL^{-1} (curve b) and 1.5 pg mL^{-1} (curve c) concentration of Cu^{2+}.

Cu^{2+}. In addition, the N_2 adsorption desorption isotherm and the Barrett-Joyner-Halenda (BJH) pore distribution (Fig. 4D) of MSNs demonstrated that the excellent BET surface area and well-defined pore size (2.8 nm), which guaranteed the efficient loading of Cu^{2+}. Furthermore, in order to investigated the stability of ssDNAs encapsulation Cu^{2+} loaded PMSNs, i-*t*-tests were carried out (Fig. S8). As shown, no obvious current change occurred until the introduction of cTnI, implying that the pores of PMSNs could be well blocked by ssDNAs and nearly no leakage of Cu^{2+}.

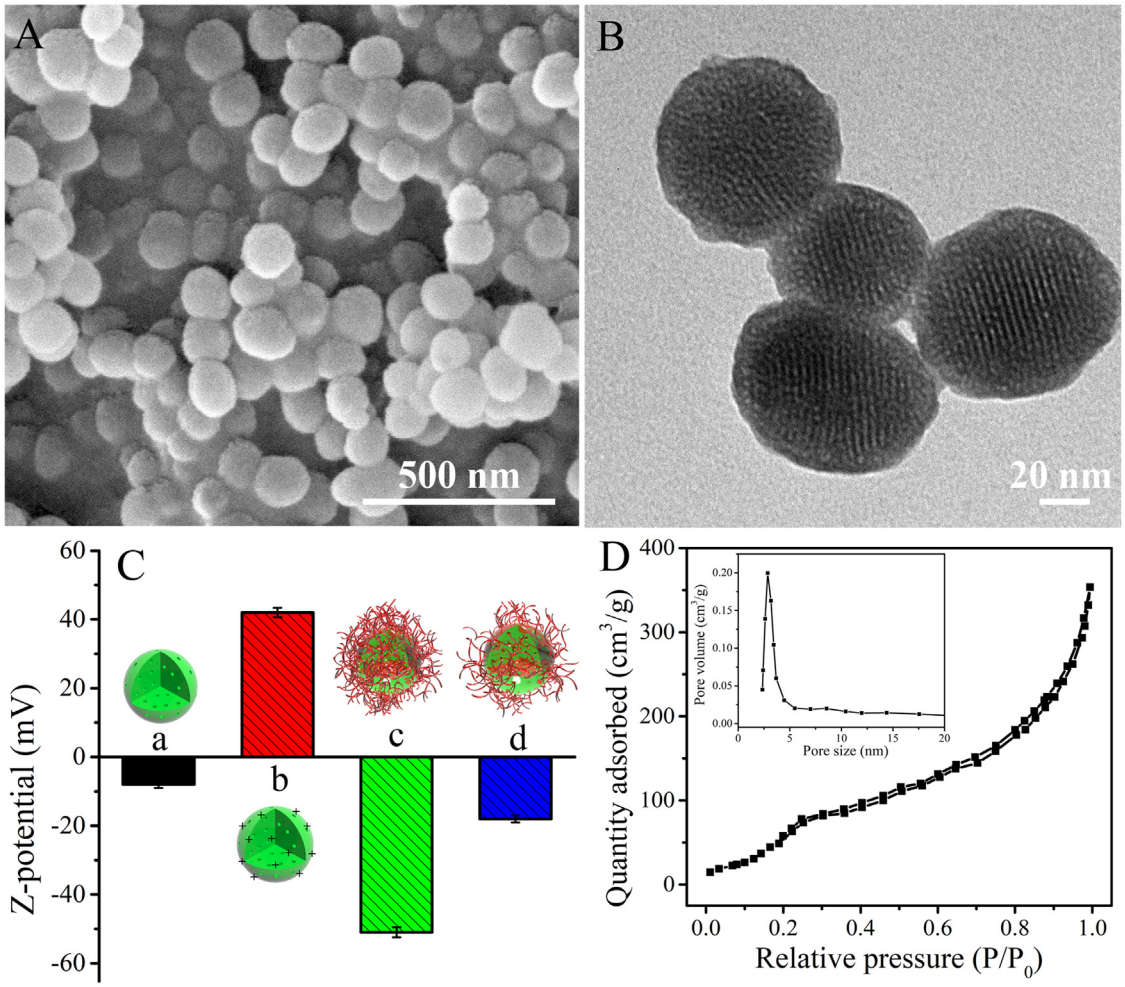

Fig. 4. SEM (A) and TEM (B) images of MSNs. (C) zeta potential of MSNs (a), Cu^{2+} loaded PMSNs (b), Cu^{2+} loaded ssDNAs-capped PMSNs (c), and ssDNAs-capped PMSNs incubated with cTnI (d). (D) N_2 adsorption-desorption isotherm of MSNs; Inset is the pore size distribution of MSNs.

3.5. Modification-free μ-PAD sensing of cTnI

As shown in Fig. 5A, when without cTnI, the photocurrent was higher (curve a), attributing to that the photocurrent quencher of Cu^{2+} was sealed in the PMSNs and could not consume the CdS photoactive material. However, when with cTnI, the ssDNAs were liberated from the surface of PMSNs, and then the bio-gate was opened, resulting in the releasing of Cu^{2+} and a relatively lower photocurrents were obtained (curves a to j), confirming the feasibility of the target-induced strategy, and thus the modification-free μ-PAD was indeed achieved. Moreover, the photocurrent intensities gradually decreased with the elevated cTnI concentrations ranging from 1.2 fg mL^{-1} to 20 ng mL^{-1} (Fig. 5B). The linear equation was $I = 410.95–54.42 \log(c/\text{pg mL}^{-1})$, with a correlation coefficient of 0.994, where I was the photocurrent intensity and c was the concentration of cTnI. The limit of detection (LOD) was 0.47 fg mL^{-1}. In addition, as shown in Table S2, the

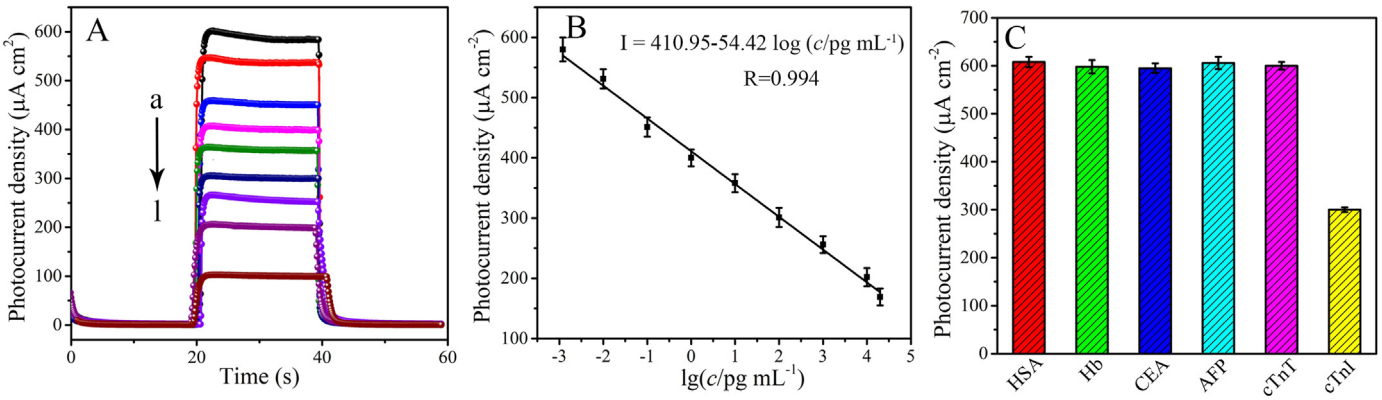

Fig. 5. (A) Photocurrent intensities of modification-free μ-PAD in the presence of different cTnI concentrations (a~j: 0.0012, 0.01, 0.1, 1, 10, 100, 1000, 10000, 20000 pg mL^{-1}). (B) Linear calibration curve of photocurrent density toward the concentration of cTnI. (C) Photocurrent responses of the μ-PAD toward various interfering of cTnT, HAS, Hb, CEA, and AFP with the concentration of 100 pg mL^{-1}.

designed μ-PAD exhibited great performance towards the detection of cTnI.

3.6. Specificity, reproducibility, and stability of the μ-PAD

To assess the specificity of the modification-free μ-PAD, cardiac troponin-T (cTnT), human serum albumin (HSA), hemoglobin (Hb), carcinoembryonic antigen (CEA), and α-1-fetoprotein (AFP) with the concentration of 100 pg mL^{-1} were used as the interfering substances. Fig. 5C showed that when with the interfering, the photocurrent densities were almost same and much higher than that of the target cTnI due to the interfering could not specific recognition with the bio-gate of ssDNAs and no Cu^{2+} was released. When with cTnI, the bio-gate could be opened and the signal quencher of Cu^{2+} was released, which could reduce the photocurrent density, implying the good specificity of the designed μ-PAD for discriminating cTnI. What's more, the reproducibility was evaluated with intra- and inter-assay precision with six independent devices. The relative standard deviations (RSD) of photocurrent response were 5.2% and 4.5% for intra- and inter-assay, respectively, which demonstrated that the acceptable reproducibility. Furthermore, the stability was investigated with the intermittent photocurrent response tests. No obvious change was observed after storing for 6 weeks at 4 °C, indicating the acceptable stability of the μ-PAD, as shown in Fig. S9.

3.7. cTnI detection in serum samples

In order to evaluate the application potential of the modification-free μ-PAD, a recovery experiment was carried out. cTnI with various concentrations were added into human serum and detected using the μ-PAD. As shown in Table S3, the recoveries were from 92.8% to 108.6%, suggesting the good potential application of the designed μ-PAD for clinical determination.

4. Conclusion

In this work, an efficient modification-free μ-PAD based on the target-induced Cu^{2+} controlled release was designed for cTnI detection for the first time. Single-crystalline PSATs were prepared as the highways for the charge carriers transfer, and the formation of PSATs/CdS heterojunctions were operated to extend the solar spectrum response. The PMSNs with the well-defined nanoporous were used as the nanocarrier to efficient entrap signal quencher of Cu^{2+}, and ssDNAs were used as the bio-gate to encapsulate the Cu^{2+} inside PMSNs. The target analyte of cTnI could be specific interacted with ssDNAs, triggering the releasing of Cu^{2+} in a controlled way, which could further reaction with CdS and eventually decrease the photocurrent signal. In this way, the photocurrent was directly related to the amount of Cu^{2+}, and was reflected to the concentration of cTnI. The obtained novel label-free and modification-free μ-PAD not only provided an ingenious idea for realizing simple, portable, and ultrasensitive bioassays but also had a great potential to be adopted as a powerful tool for precision medicine.

CRediT authorship contribution statement

Chaomin Gao: Conceptualization, Methodology, Writing - original draft. **Jie Xue:** Investigation, Formal analysis. **Lina Zhang:** Visualization, Data curation. **Peini Zhao:** Resources, Visualization. **Kang Cui:** Writing - review & editing, Resources. **Shenguang Ge:** Supervision, Funding acquisition. **Jinghua Yu:** Funding acquisition, Project administration.

Acknowledgments

This work was Financial supports form the National Natural Science Foundation of China (Grants 21874055, 51872121, 21775055), the program for Taishan Scholars of Shandong Province (Grant ts201712048), and the 111 Project of International Corporation on Advanced Cement-based Materials (Grant No. D17001).

Declaration of interests

The authors declare that they have no known competing financial interests or personal relationships that could have appeared to influence the work reported in this paper.

Appendix A. Supplementary material

Supplementary data associated with this article can be found in the online version at doi:10.1016/j.bios.2019.01.038.

References

Ai, G.J., Mo, R., Li, H.X., Zhong, J.X., 2015. Nanoscale 7, 6722–6728.
Awate, S.V., Deshpande, S.S., Rakesh, K., Dhanasekaran, P., Gupta, N.M., 2011. Phys. Chem. Chem. Phys. 13, 11329–11339.
Butburee, T., Bai, Y., Wang, H.J., Chen, H.J., Wang, Z.L., Liu, G., Zou, J., Khemthong, P., Max, Lu, G.Q., Wang, L.Z., 2018. Adv. Mater. 30, 1705666.
Cate, D.M., Adkins, J.A., Mettakoonpitak, J., Henry, C.S., 2014. Anal. Chem. 87, 19–41.
Chang, K.W., Wu, J.J., 2005. Adv. Mater. 17, 241–245.
Du, Y.P., Chen, B., Yin, Z., Liu, Z.Q., Zhang, H., 2014. small 10, 4727–4734.
Gai, P.P., Gu, C.C., Hou, T., Li, F., 2018. ACS Appl. Mater. Interfaces 10, 9325–9331.
Gao, C.M., Su, M., Wang, Y.H., Ge, S.G., Yu, J.H., 2015. RSC Adv. 5, 28324–28331.
Gao, C.M., Yuan, S., Cui, K., Qiu, Z.W., Ge, S.G., Cao, B.Q., Yu, J.H., 2018a. Sol. RRL 11, 1800175.
Gao, H.M., Zhang, D.Y., Yang, M.N., Dong, S., 2017. Sol. RRL 1, 1700183.
Gao, C.M., Xue, J., Zhang, L.N., Cui, K., Li, H., Yu, J.H., 2018b. Anal. Chem. 90, 14116–14120.
Gu, C., Gai, P.P., Hou, T., Li, H., Xue, C., Li, F., 2017. ACS Appl. Mater. Interfaces 9, 35721–35728.
He, Q., Wan, Y.Y., Zhang, Y.K., Jiang, H.L., Liu, H.J., Zheng, X.S., Chen, S.M., Wu, X.J., Song, L., 2018. Sol. RRL 2, 1800032.
Kokkinos, C.T., Giokas, D.L., Economou, A.S., Petrou, P.S., Kakabakos, S.E., 2018. Anal. Chem. 90, 1092–1097.
Korff, S., Katus, H.A., Giannitsis, E., 2006. Heart 92, 987–993.
Lee, J.S., Joung, H.A., Kim, M.G., Park, C.B., 2012. ACS Nano 6, 2978–2983.
Li, G.S., Zhang, D.Q., Yu, J.C., 2009. Environ. Sci. Technol. 43, 7079–7085.
Li, D., Duan, H., Ma, Y., Deng, W., 2018. Anal. Chem. 90, 5719–5727.
Li, S.X., Lin, X.F., Zheng, F.Y., Liang, W.J., Zhong, Y.X., Cai, J.B., 2014a. Anal. Chem. 86, 7079–7083.
Li, X., Wang, Y.H., Zhao, C., Liu, X.Y., 2014b. ACS Appl. Mater. Interfaces 6, 22004–22012.
Liu, Y.B., Yao, Q.F., Wu, X.J., Chen, T.K., Ma, Y., Ong, C.N., Xie, J.P., 2016. Nanoscale 8, 10145–10151.
Martinez, A.W., Phillips, S.T., Butte, M.J., Whitesides, G.M., 2007. Angew. Chem. Int. Ed. 46, 1318–1320.
Mei, L.P., Jiang, X.Y., Yu, X.D., Zhao, W.W., Xu, J.J., Chen, H.Y., 2018. Anal. Chem. 90, 2749–2755.
Muller, R., Zanotto, E.D., Fokin, V.M., 2000. J. Non-Cryst. Solids 274, 208–231.
Scala-Benuzzi, M.L., Raba, J., Soler-Illia, G., Schneider, R.J., Messina, G.A., 2018. Anal. Chem. 90, 4104–4111.
Wang, G.L., Xu, J.J., Chen, H.Y., 2010. Nanoscale 2, 1112–1114.
Wang, J., Li, X.L., Zhang, J.D., Hao, N., Xu, J.J., Chen, H.Y., 2015. Chem. Commun. 51, 11673–11676.
Wang, S.W., Ge, L., Song, X.R., Yan, M., Ge, S.G., Yu, J.H., Zeng, F., 2012. Analyst 137, 3821–3827.
Wang, Z.H., Tammela, P., Strømme, M., Nyholm, L., 2017. Adv. Energy Mater. 7, 1700130.
Wu, N.Q., Wang, J., Tafen, D.N., Wang, H., Zheng, J.G., Lewis, J.P., Liu, X.G., Leonard, S.S., Manivannan, A., 2010. J. Am. Chem. Soc. 132, 6679–6685.
Xu, T., Hou, W., Shen, X., Wu, H., Li, X., Wang, J., Jiang, Z., 2011. J. Power Sources 196, 4934–4942.
Yang, W.Q., Ni, J.C., Luo, F., Weng, W., Wei, Q.H., Lin, Z.Y., Chen, G.N., 2017. Anal. Chem. 89, 8384–8390.
Yu, J.H., Ge, L., Huang, J.D., Wang, S.W., Ge, S.G., 2011. Lab Chip 11, 1286–1291.
Yu, Z.G., Lai, R.Y., 2013. Anal. Chem. 85, 3340–3346.
Zhang, B., Liu, B.L., Liao, J.Y., Chen, G.N., Tang, D.P., 2013. Anal. Chem. 85, 9245–9252.
Zhuang, T.T., Liu, Y., Li, Y., Zhao, Y., Wu, L., Jiang, J., Yu, S.H., 2016. Angew. Chem. Int. Ed. 55, 6396–6400.